Prediction of interfacial debonding between stiff spherical particles and a soft matrix with the coupled criterion

E. Martin, Dominique Leguillon, A. Catapano, Nicolas Carrère

Prediction of interfacial debonding between stiff spherical particles and a soft matrix with the coupled criterion

E. Martin[1*], D. Leguillon[2], A. Catapano[3], N. Carrère[4]

[1] LCTS, Bordeaux INP, Université de Bordeaux, CNRS UMR 5801, Pessac, France

[2] IJLRA, Sorbonne Université, CNRS UMR 7190, Paris, France

[3] I2M, Bordeaux INP, Université de Bordeaux, CNRS UMR 5295, Talence, France

[4] IRDL, ENSTA Bretagne, UMR CNRS UMR 6027, Brest, France

* Corresponding author: martin@lcts.u-bordeaux.fr

Abstract

The tensile load at debonding onset between stiff particles and a soft matrix is predicted with the coupled criterion which combines a stress and an energy conditions. A finite element model of a representative volume element is implemented in order to consider the influence of the size of the particles, the particle volume fraction, mixed mode conditions at the interface and the presence of residual stresses. It is also shown how this approach can be used in order to analyze experimental data for the identification of the interfacial fracture parameters.

Keywords : Particle reinforced polymer; Interfacial debonding; Coupled criterion; Finite Fracture Mechanics;

1. Introduction

Reinforcing a matrix with rigid particles is an attractive way to increase its mechanical properties. Spherical particles have been demonstrated to improve the stiffness, tensile strength, and toughness of polymeric and ceramic matrices [1-4]. Enhancement of the global mechanical properties of these composites depend on the component properties and their volume fractions but also on the strength and toughness of the interface between the matrix and the particles.

For polymer filled with stiff particles, there is a consensus that interfacial debonding which facilitates matrix shear yielding is a pre-requisite to obtain high toughness [2, 5]. As verified experimentally under tensile loading [6-10], at debonding onset, an area first develops instantaneously from the poles of the particles and extends progressively along the interface with increasing applied stress. Previous works [11] estimate the debonding stress σ_D by evaluating the energy necessary to create the debonding area with

$$\sigma_D = C\sqrt{\frac{G_i^c}{R}} - \frac{\sigma^T}{2} \tag{1}$$

where G_i^c is the interfacial fracture energy, R is the particle radius, σ^T is the thermal stress resulting from the thermal expansion mismatch between the particles and the matrix, C is a coefficient depending on component properties. Eq. (1) shows that the debonding stress exhibits a size effect as it depends on the particle radius. Comparing σ_D with the composite tensile strength indicates that there is a critical size below which no interface debonding and thus little toughening can develop. Similar expressions were derived for a hydrostatic loading [2, 5, 12-14] but it must be noted that the value of the debonding surface is always postulated or taken as the complete interfacial area. To get rid of this assumption, only justified under hydrostatic loading, a finite fracture approach can be used as already demonstrated by several authors [15-16]. More precisely, combining a stress and an energy conditions gives access to

the debond stress and the debonding area. The present work uses such a coupled criterion to describe the nucleation of interfacial debonding between stiff particles and a soft matrix. The previous studies are now extended by considering the particle volume fraction and taking into account the presence of residual stresses.

The paper is organized as follows: the coupled criterion is outlined in Section 2 while Section 3 examines the choice of a proper representative cell. Numerical results are presented in Section 4 including the influence of mixed mode conditions and residual stresses. Section 5 is devoted to the analysis of experimental results.

2. Prediction of interfacial debonding

The geometry considered for the presentation of this section is the one that will be analyzed afterwards: a spherical particle (radius *R*) embedded in a matrix and submitted to a tensile loading σ in the *z* direction (Fig. 1a). A given point at the particle/matrix interface is located by the angle θ measured from the *z* axis. Particle and matrix are elastic and isotropic materials with Young's moduli $\left(E_p, E_m\right)$ and Poisson's ratios $\left(\upsilon_p, \upsilon_m\right)$. It is assumed that the particle is stiffer than the matrix with $E_p > E_m$. This elastic mismatch induces a stress concentration along the interface around the top and bottom poles. Upon a critical loading, two symmetric debonds (angle θ_D) are nucleated at the poles (Fig. 1b). Experimental observations may indicate that interfacial debonding occurs firstly at one pole followed shortly by a second crack initiated at the other pole of the same particle. In any case, the difference in predicted applied stress between both debonded modes is weak as shown by García *et al.* [15].

Assuming a brittle behavior of the interface, the coupled criterion (CC) which combines an energy and a stress conditions is used to describe the initiation of this interfacial fracture mechanism [17, 18]:

a) The energy condition requires the change in potential energy $\delta\,\Pi$ to be larger than the energy necessary for the nucleation of the interfacial crack of surface $S(\theta)$ with

$$-\delta\,\Pi = \Pi(0) - \Pi\left(S(\theta)\right) \geq S(\theta) G_i^c\,, \tag{2}$$

where G_i^c is the interfacial fracture energy. Note that the constant G_i^c denotes here a generic parameter that will be specified in Section 4.1 taking into account the concept of mixed-mode. Eq. (2) can be written in order to introduce the incremental energy release rate (IERR) $G_{inc}\left(S(\theta)\right) = -\delta\,\Pi / S(\theta)$ leading to

$$G_{inc}\left(S(\theta)\right) \geq G_i^c\,. \tag{3}$$

The relationship between the IERR and the differential energy release rate $G_i(S) = -d\Pi/dS$ is [19]

$$G_{inc}(S(\theta)) = \frac{1}{S(\theta)} \int_0^{S(\theta)} G_i(A)\, dA\,, \tag{4}$$

which induces

$$S \frac{dG_{inc}(S)}{dS} = G_i(S) - G_{inc}(S)\,, \tag{5}$$

where θ has been omitted in the expression of S for sake of simplicity.

b) The stress condition stipulates that the opening normal stress all along the anticipated crack path must exceed the interfacial strength σ_i^c. A local coordinate system (x, y) along the interface is used to define $\vec{x}$ as the normal direction and the stress condition is expressed as

$$\sigma_{xx}(\alpha) \geq \sigma_i^c \quad \text{for } \alpha \leq \theta\,. \tag{6}$$

A similar inequality is valid for mixed-mode, σ_i^c is then a generic constant and the role of tensile and shear strengths will be specified further in Section 4.1.

Eq. (3) and (6) are the CC inequalities that must be solved to determine the applied tensile stress σ_D and the angle θ_D at onset of debonding. They can be modified to take into account mixed-mode condition or thermal residual stresses as will be shown in section 4.

3. Selection of a Representative Volume Element (RVE)

As recently pointed out [20], the CC can be implemented with the help of a matched asymptotic approach or a full finite element approach. A full field finite element analysis is used here but we mention that the matched asymptotic approach may also be used for very small values of the particle volume fraction [21]. To avoid time-consuming 3D calculations, we have opted for 2D calculations based on axial symmetry. The simplest of the volumes we can consider contains a single particle. The major challenge is then to choose a model that takes satisfactorily into account the interactions between neighboring particles. We must also determine how to evaluate the change in potential energy necessary to apply the energy condition.

3.1 The spherical RVE

The simplest shape of the RVE is made of two concentric spheres. Taking into account the axial symmetry and the symmetry of geometry and loading, the RVE reduces to two concentric quarter of disk as shown in Fig. 2a. For the sake of simplicity, the radius of the inner disk is set to 1 (with the appropriate changes in the equations), and the dimensionless outer one is $R_{\mathrm{m}} = 1/V_{\mathrm{P}}^{1/3}$, where V_{P} is the volume fraction of particles. Along the Oz axis, no conditions have to be prescribed due to the axial symmetry formulation of the problem. Along the Or axis (Fig. 1), usual symmetry conditions are applied to the displacement field $\underline{U}$ and stress field $\underline{\underline{\sigma}}$

$$U_z = 0 \quad \sigma_{rz} = 0 \text{ on } Or \text{ (the horizontal axis).} \tag{7}$$

To simulate the remote loading, a unit macroscopic strain $\varepsilon_{zz} = 1$ is prescribed along the outer circle Γ_{out} by imposing

$$U_z = z\,. \tag{8}$$

Theoretically, there exists an alternative approach prescribing a force corresponding to a unit unidirectional stress field $\sigma_{zz} = 1$ but it has been checked that it is not as effective. For the thermal loading, the outer circle remains free of forces reflecting the fact that the macroscopic (homogenized) stress field is zero.

Let us define the following functional spaces

$$\begin{aligned}
\boldsymbol{\mathcal{U}} &= \left\{\underline{W} \in \mathrm{H}_1(\Omega),\ W_z = 0 \text{ on } Or,\ W_z = z \text{ on } \Gamma_{out}\right\},\\
\boldsymbol{\mathcal{U}}_0 &= \left\{\underline{W} \in \mathrm{H}_1(\Omega),\ W_z = 0 \text{ on } Or,\ W_z = 0 \text{ on } \Gamma_{out}\right\},\\
\boldsymbol{\mathcal{V}} &= \left\{\underline{W} \in \mathrm{H}_1(\Omega),\ W_z = 0 \text{ on } Or\right\}.
\end{aligned}$$

Here $\mathrm{H}_1(\Omega)$ is the Sobolev space ensuring enough smoothness and integrability to the functions over the whole domain Ω (i.e. the domain filled by the RVE). The variational formulation for an auxiliary elastic problem with prescribed strain can be written

Find $\underline{W}^{\mathrm{el}} \in \boldsymbol{\mathcal{U}}$ such that

$$\int_\Omega \mathbf{C} : \nabla \underline{W}^{\mathrm{el}} : \nabla \underline{V}\ \mathrm{d}s = 0 \quad \forall \underline{V} \in \boldsymbol{\mathcal{U}}_0\,, \tag{9}$$

where $\mathbf{C}$ is the elastic fourth order tensor and where the generic element of surface ds denotes of course the weighted integration element r dr dz taking into account the axial symmetry of Ω. The variational formulation for the auxiliary thermo-elastic problem (pure residual stresses without any mechanical loading) can be written

Find $\underline{W}^{\mathrm{th}} \in \boldsymbol{\mathcal{V}}$ such that

$$\int_\Omega \mathbf{C} : \nabla \underline{W}^{\mathrm{th}} : \nabla \underline{V}\ \mathrm{d}s = \int_\Omega \mathbf{C} : \underline{\underline{\varepsilon}}^{\mathrm{in}} : \nabla \underline{V}\ \mathrm{d}s \quad \forall \underline{V} \in \boldsymbol{\mathcal{V}}\ , \tag{10}$$

with $\underline{\underline{\varepsilon}}^{\text{in}} = \alpha \underline{\underline{I}}$ (a unit temperature change) where α is the coefficient of thermal expansion (CTE) and $\underline{\underline{I}}$ the second order identity tensor.

The actual solution is then

$$\underline{U} = \varepsilon_{zz} \underline{W}^{\text{el}} + \Delta T \underline{W}^{\text{th}} \ , \tag{11}$$

where ε_{zz} is the remote strain and ΔT the actual temperature change. The potential energy associated with $\underline{U}$ can be expressed as

$$\begin{aligned} \Pi &= \frac{1}{2}\int_\Omega \mathbf{C} : \left(\nabla \underline{U} - \Delta T \underline{\underline{\varepsilon}}^{\text{in}}\right) : \left(\nabla \underline{U} - \Delta T \underline{\underline{\varepsilon}}^{\text{in}}\right) \mathrm{d}s \\ &= \frac{\varepsilon_{zz}^2}{2}\int_\Omega \mathbf{C} : \nabla \underline{W}^{\text{el}} : \nabla \underline{W}^{\text{el}} \mathrm{d}s + \frac{\Delta T^2}{2}\int_\Omega \mathbf{C} : \left(\nabla \underline{W}^{\text{th}} - \underline{\underline{\varepsilon}}^{\text{in}}\right) : \left(\nabla \underline{W}^{\text{th}} - \underline{\underline{\varepsilon}}^{\text{in}}\right) \mathrm{d}s \\ &\quad + \varepsilon_{zz} \Delta T \int_\Omega \mathbf{C} : \nabla \underline{W}^{\text{el}} : \left(\nabla \underline{W}^{\text{th}} - \underline{\underline{\varepsilon}}^{\text{in}}\right) \mathrm{d}s. \end{aligned} \tag{12}$$

The last term vanish as a consequence of Eq. (10) and the nesting of the functional spaces, then

$$\begin{aligned} \Pi &= \frac{\varepsilon_{zz}^2}{2}\int_\Omega \mathbf{C} : \nabla \underline{W}^{\text{el}} : \nabla \underline{W}^{\text{el}} \mathrm{d}s + \frac{\Delta T^2}{2}\int_\Omega \mathbf{C} : \left(\nabla \underline{W}^{\text{th}} - \underline{\underline{\varepsilon}}^{\text{in}}\right) : \left(\nabla \underline{W}^{\text{th}} - \underline{\underline{\varepsilon}}^{\text{in}}\right) \mathrm{d}s \\ &= \frac{\varepsilon_{zz}^2}{2}\int_\Omega \mathbf{C} : \nabla \underline{W}^{\text{el}} : \nabla \underline{W}^{\text{el}} \mathrm{d}s + \frac{\Delta T^2}{2}\int_\Omega \mathbf{C} : \nabla \underline{W}^{\text{th}} : \nabla \underline{W}^{\text{th}} \mathrm{d}s + \frac{\Delta T^2}{2}\int_\Omega \mathbf{C} : \underline{\underline{\varepsilon}}^{\text{in}} : \underline{\underline{\varepsilon}}^{\text{in}} \mathrm{d}s \\ &\quad - \Delta T^2 \int_\Omega \mathbf{C} : \nabla \underline{W}^{\text{th}} : \underline{\underline{\varepsilon}}^{\text{in}} \mathrm{d}s \\ &= \frac{\varepsilon_{zz}^2}{2}\int_\Omega \mathbf{C} : \nabla \underline{W}^{\text{el}} : \nabla \underline{W}^{\text{el}} \mathrm{d}s - \frac{\Delta T^2}{2}\int_\Omega \mathbf{C} : \nabla \underline{W}^{\text{th}} : \nabla \underline{W}^{\text{th}} \mathrm{d}s + \frac{\Delta T^2}{2}\int_\Omega \mathbf{C} : \underline{\underline{\varepsilon}}^{\text{in}} : \underline{\underline{\varepsilon}}^{\text{in}} \mathrm{d}s. \end{aligned} \tag{13}$$

The last term is unchanged for two states of the representative cell, i.e. with or without debonding, thus the change in potential energy is (δ should be read “the change of”)

$$\delta\, \Pi = \frac{\varepsilon_{zz}^2}{2}\delta\int_\Omega \mathbf{C} : \nabla \underline{W}^{\text{el}} : \nabla \underline{W}^{\text{el}} \mathrm{d}s - \frac{\Delta T^2}{2}\delta\int_\Omega \mathbf{C} : \nabla \underline{W}^{\text{th}} : \nabla \underline{W}^{\text{th}} \mathrm{d}s. \tag{14}$$

Once (9) and (10) are discretized by finite elements, this term can be computed

$$\delta\, \Pi = \frac{\varepsilon_{zz}^2}{2}\delta \mathbb{K} \mathbf{X}^{\text{el}} \mathbf{X}^{\text{el}} - \frac{\Delta T^2}{2}\delta \mathbb{K} \mathbf{X}^{\text{th}} \mathbf{X}^{\text{th}}. \tag{15}$$

where $\mathbb{K}$ is the stiffness matrix of the discretized systems, the same in both cases, $\mathbf{X}^{\text{el}}$ and $\mathbf{X}^{\text{th}}$ are the vectors of nodal unknowns of the auxiliary elastic and thermo-elastic problems.

Eq. (15) shows a very simple form without coupling terms, easy to implement. Unfortunately, as seen further when comparing with results from experiments, this spherical RVE works well only for small volume fraction of particles. Indeed, such a RVE is very convenient and commonly used in homogenization but does not really takes into account the interaction between neighboring particles.

3.2 The cylindrical RVE

An alternative is to select a cylindrical RVE (Fig. 2b). The radius of the cylinder being equal to the half-height to preserve the distance between particles. The symmetry conditions are the same as above, then the RVE reduces to a square with dimensionless half side $R_{\mathrm{m}} = (2/3V_{\mathrm{P}})^{1/3}$ embedding the quarter disk with radius 1 that represents the particle.

Now the boundary conditions on the upper Γ_{T} and lateral Γ_{R} boundaries should reflect both the remote load and the proximity of neighboring cells. To ensure the latter condition and taking into account the symmetries of the mechanical and thermal loadings, the upper and lateral faces must remain straight and move parallel to themselves. To this aim let us first define the following functional spaces

$$\begin{aligned}
\boldsymbol{\mathcal{U}}^r &= \{\underline{W} \in \mathrm{H}_1(\Omega),\ W_z = 0 \text{ on } Or,\ W_z = 0 \text{ on } \Gamma_T,\ W_r = r \text{ on } \Gamma_{\mathrm{R}}\},\\
\boldsymbol{\mathcal{U}}^z &= \{\underline{W} \in \mathrm{H}_1(\Omega),\ W_z = 0 \text{ on } Or,\ W_z = z \text{ on } \Gamma_T,\ W_r = 0 \text{ on } \Gamma_{\mathrm{R}}\},\\
\boldsymbol{\mathcal{U}}^0 &= \{\underline{W} \in \mathrm{H}_1(\Omega),\ W_z = 0 \text{ on } Or,\ W_z = 0 \text{ on } \Gamma_{\mathrm{T}},\ W_r = 0 \text{ on } \Gamma_{\mathrm{R}}\}.
\end{aligned}$$

Two auxiliary elastic problems are defined as

Find $\underline{W}^r \in \boldsymbol{\mathcal{U}}^r$ such that

$$\int_\Omega \mathbf{C} : \nabla \underline{W}^r : \nabla \underline{V}\ \mathrm{d}s = 0 \quad \forall \underline{V} \in \boldsymbol{\mathcal{U}}^0\ . \tag{16}$$

Find $\underline{W}^z \in \boldsymbol{\mathcal{U}}^z$ such that

$$\int_\Omega \mathbf{C} : \nabla \underline{W}^z : \nabla \underline{V} \, \mathrm{d}s = 0 \quad \forall \underline{V} \in \boldsymbol{\mathcal{U}}^0 . \tag{17}$$

The solution to the elastic problem can be written

$$\underline{U}^{\mathrm{el}} = a_r \underline{W}^r + \varepsilon_{zz} \underline{W}^z \ , \tag{18}$$

where ε_{zz} is the remote prescribed strain and where a_r is obtained imposing a vanishing horizontal resultant force, reflecting the fact that the lateral boundaries of the specimen remain free

$$R_r(\underline{U}^{\mathrm{el}}) = a_r R_r(\underline{W}^r) + \varepsilon_{zz} R_r(\underline{W}^z) = 0 \ , \tag{19}$$

here R_r holds for the resultant force in the Or direction.

Let $\underline{W}^{\mathrm{th}}$ be the solution to the auxiliary thermo-elastic problem with a unit temperature change, the upper and lateral faces being fixed (i.e. 0 displacements)

Find $\underline{W}^{\mathrm{th}} \in \boldsymbol{\mathcal{U}}^0$ such that

$$\int_\Omega \mathbf{C} : \nabla \underline{W}^{\mathrm{th}} : \nabla \underline{V} \, \mathrm{d}s = \int_\Omega \mathbf{C} : \underline{\underline{\varepsilon}}^{\mathrm{in}} : \nabla \underline{V} \, \mathrm{d}s \quad \forall \underline{V} \in \mathrm{U}^0 \ . \tag{20}$$

The solution to the thermo-elastic problem can be written

$$\underline{U}^{\mathrm{th}} = \Delta T \ \underline{W}^{\mathrm{th}} + b_r \underline{W}^r + b_z \underline{W}^z \ . \tag{21}$$

The coefficients b_r and b_z are determined such that horizontal and vertical resultant forces vanish, reflecting, as above, the fact that the macroscopic (homogenized) stress field is zero

$$\begin{aligned} R_r(\underline{U}^{\mathrm{th}}) &= b_r R_r(\underline{W}^r) + b_z R_r(\underline{W}^z) = 0, \\ R_z(\underline{U}^{\mathrm{th}}) &= b_r R_z(\underline{W}^r) + b_z R_z(\underline{W}^z) = 0. \end{aligned} \tag{22}$$

The full solution can be written

$$\begin{aligned} &\underline{U} = \underline{U}^{\mathrm{th}} + \underline{U}^{\mathrm{el}} = \Delta T \ \underline{W}^{\mathrm{th}} + A_r \underline{W}^r + A_z \underline{W}^z \\ &\text{with } A_r = a_r + b_r \ \text{ and } \ A_z = \varepsilon_{zz} + b_z . \end{aligned} \tag{23}$$

The change in potential energy $\delta \Pi$ is

$$\begin{aligned}\delta\,\Pi &= \frac{1}{2}\delta\int_\Omega \mathbf{C} : (\nabla\underline{U} - \Delta T\,\underline{\underline{\varepsilon}}^{\text{in}}) : (\nabla\underline{U} - \Delta T\,\underline{\underline{\varepsilon}}^{\text{in}})\ \mathrm{d}s \\ &= \frac{1}{2}\delta\int_\Omega \mathbf{C} : \nabla\underline{U} : \nabla\underline{U}\ \mathrm{d}s - \Delta T\ \delta\int_\Omega \mathbf{C} : \underline{\underline{\varepsilon}}^{\text{in}} : \nabla\underline{U}\ \mathrm{d}s + \frac{\Delta T^2}{2}\delta\int_\Omega \mathbf{C} : \underline{\underline{\varepsilon}}^{\text{in}} : \underline{\underline{\varepsilon}}^{\text{in}}\ \mathrm{d}s.\end{aligned} \tag{24}$$

The last term vanishes because it does not change between the two states (without and with debonding) of the RVE, then substituting Eq. (23) leads to

$$\begin{aligned}\delta\,\Pi = {} & \frac{\Delta T^2}{2}\delta\int_\Omega \mathbf{C} : \nabla\underline{W}^{\text{th}} : \nabla\underline{W}^{\text{th}}\ \mathrm{d}s + \frac{A_r^2}{2}\delta\int_\Omega \mathbf{C} : \nabla\underline{W}^{r} : \nabla\underline{W}^{r}\ \mathrm{d}s \\ & + \frac{A_z^2}{2}\delta\int_\Omega \mathbf{C} : \nabla\underline{W}^{z} : \nabla\underline{W}^{z}\ \mathrm{d}s + A_r A_z\delta\int_\Omega \mathbf{C} : \nabla\underline{W}^{r} : \nabla\underline{W}^{z}\ \mathrm{d}s \\ & - \Delta T^2\ \delta\int_\Omega \mathbf{C} : \underline{\underline{\varepsilon}}^{\text{in}} : \nabla\underline{W}^{\text{th}}\ \mathrm{d}s - \Delta T\ A_r\delta\int_\Omega \mathbf{C} : \underline{\underline{\varepsilon}}^{\text{in}} : \nabla\underline{W}^{r}\ \mathrm{d}s - \Delta T\ A_z\delta\int_\Omega \mathbf{C} : \underline{\underline{\varepsilon}}^{\text{in}} : \nabla\underline{W}^{z}\ \mathrm{d}s.\end{aligned} \tag{25}$$

and finally

$$\begin{aligned}\delta\Pi = {} & -\frac{\Delta T^2}{2}\delta\int_\Omega \mathbf{C} : \nabla\underline{W}^{\text{th}} : \nabla\underline{W}^{\text{th}}\ \mathrm{d}s + \frac{A_r^2}{2}\delta\int_\Omega \mathbf{C} : \nabla\underline{W}^{r} : \nabla\underline{W}^{r}\ \mathrm{d}s \\ & + \frac{A_z^2}{2}\delta\int_\Omega \mathbf{C} : \nabla\underline{W}^{z} : \nabla\underline{W}^{z}\ \mathrm{d}s + A_r A_z\delta\int_\Omega \mathbf{C} : \nabla\underline{W}^{r} : \nabla\underline{W}^{z}\ \mathrm{d}s \\ & - \Delta T\ A_r\delta\int_\Omega \mathbf{C} : \underline{\underline{\varepsilon}}^{\text{in}} : \nabla\underline{W}^{r}\ \mathrm{d}s - \Delta T\ A_z\delta\int_\Omega \mathbf{C} : \underline{\underline{\varepsilon}}^{\text{in}} : \nabla\underline{W}^{z}\ \mathrm{d}s.\end{aligned} \tag{26}$$

Using the previous notations, $\mathbf{X}^r$, $\mathbf{X}^z$ et $\mathbf{X}^{\text{th}}$ being the vectors of nodal unknowns associated respectively with $\underline{W}^r$, $\underline{W}^z$ et $\underline{W}^{\text{th}}$ and $\mathbf{B}$ being the right hand side vector of the thermo-elastic system Eq. (20), it comes

$$\begin{aligned}\delta\,\Pi = {} & -\frac{\Delta T^2}{2}\delta\mathbb{K}\mathbf{X}^{\text{th}}\mathbf{X}^{\text{th}} + \delta\frac{A_r^2}{2}\mathbf{X}^r\mathbf{X}^r + \delta\frac{A_z^2}{2}\mathbb{K}\mathbf{X}^z\mathbf{X}^z + \delta A_r A_z\mathbb{K}\mathbf{X}^r\mathbf{X}^z \\ & - \Delta T\delta A_r\mathbf{B}\mathbf{X}^r - \Delta T\delta A_z\mathbf{B}\mathbf{X}^z.\end{aligned} \tag{27}$$

Even if each term is rather simple and can be easily computed, it may be better, first to combine the terms applying Eq. (23) and then to use Eq. (24) to compute the change in potential energy

$$\begin{aligned}\mathbf{X} &= \Delta T\ \mathbf{X}^{\text{th}} + A_r\mathbf{B}\mathbf{X}^r + A_z\mathbf{B}\mathbf{X}^z, \\ \delta\,\Pi &= \frac{1}{2}\delta\ \mathbb{K}\mathbf{X}\mathbf{X} - \Delta T\ \delta\ \mathbf{B}\mathbf{X}.\end{aligned} \tag{28}$$

In order to evaluate the efficiency of the spherical and cylindrical RVEs, prediction of Young's modulus estimated in the *z* direction as a function of the particle volume fraction is compared

with experimental data. Careful measurements of this property for a composite consisting of glass spheres embedded in epoxy resin are available in the literature [22]. Fig. 3 shows that both RVE are equivalent for $V_p < 10\%$ but the cylindrical one must be preferred for higher values. We thus adopt this axisymmetric geometry which has also been demonstrated sufficiently accurate when compared with a three-dimensional analysis [23]. However, this approach is not entirely free of drawbacks. Obviously, the Or and Oz directions are not equivalent. This is not perceptible for small volume fractions, but for larger fractions it can be seen, for example, that the tension acting along the interface in case of pure thermal loading is not strictly constant. It exhibits a slight maximum at the pole of the particle, on the Oz axis. As mentioned by previous authors [24], a particulate composite can be modeled as a matrix filled with a periodic array of particles. Assuming an hexagonal array and simplifying the hexagon to a cylinder allows to perform an axisymmetric analysis. Nevertheless, the usual conditions of the theory of homogenization are not exactly realized and it is not possible to reconstruct exactly the entire structure by repeating the pattern formed by the RVE.

4. Numerical results

Finite element calculations are now performed with the cylindrical RVE in order to estimate the applied stress at decohesion onset using the CC.

4.1 Single mode failure analysis

We first consider a tensile loading in the direction z. As already mentioned, the representative displacement field requires the superposition of two elastic solutions Eq. (18). The link between the CC inequalities (Eq. (3), Eq. (6)) and the applied uniaxial strain ε_{zz} is

established by introducing the stress concentration factor (SCF) $k_{xx}(\theta)$ and the dimensionless IERR $A(\theta)$ with

$$\begin{cases} \sigma_{xx}(\theta) = k_{xx}(\theta) E_i \varepsilon_{zz}, \\ G_{inc}\left(S(\theta)\right) = G_{inc}(\theta) = R E_i A(\theta) \varepsilon_{zz}^2. \end{cases} \tag{29}$$

where $E_i = 2\left[\left(1-\nu_p^2\right)/E_p + \left(1-\nu_m^2\right)/E_m\right]^{-1}$ is an interfacial effective modulus [25].

The SCF $k_{xx}\left(\theta, V_p, E_p/E_m, \nu_p, \nu_m\right)$ only requires one calculation with the perfectly bonded interface. It was checked that the finite element model allows to recover the analytical solution originated by Goodier [26] and also reported elsewhere [10, 27] for a rigid particle embedded within an infinite matrix (i.e for $V_p < 0.01\%$). The dimensionless IERR $A\left(\theta, V_p, E_p/E_m, \nu_p, \nu_m\right)$ requires several computations with a successive release of the interfacial nodes to vary the debonding length. A mesh refinement must be introduced along the selected crack path (i.e the particle/matrix interface) in order to capture accurately the angle θ_D at initiation [20]. This value is proportional to the interfacial characteristic length L_i^c as will be shown by Eq. (35). A convergence study was performed and leads to select a minimum mesh size (expressed here in terms of minimum discretized angle) $\Delta\theta < 1$ deg. provided that $L_i^c/R \geq 0.005$. A contact zone may appear near the crack tip of an interfacial crack [28]. This means that contact would take place in case of debonding and therefore further debonding cannot develop. The overlapping of crack faces was thus checked but was not detected with the selected discretization if the decohesion angle is smaller than the maximum angle θ^M which is now defined.

The stress concentration is maximum for $\theta = 0$ and k_{xx} is a decreasing function of θ. For low values of the particle volume fraction, results indicate that the SCF may become negative for $\theta \geq \theta_S^M$ with $k_{xx}\left(\theta_S^M\right) = 0$. Inversely, $A(\theta)$ exhibits a local maximum with an increase up to the angle $\theta = \theta_W^M$. As pointed out by previous authors [25,28,29], the presence

of this maximum coincides with the progressive change from mode I to mode II of the interfacial crack opening. Results reveal that $\theta_W^M < \theta_S^M$. Assuming a monotonically increasing applied strain, the energy condition Eq. (3) is first satisfied for $\theta = \theta_W^M = \theta^M$ if

$$G_{inc}\left(\theta^M\right) = RE_i A\left(\theta^M\right)\varepsilon_{zz}^2 = G_i^c . \tag{30}$$

The initiation of a debonding crack also requires the stress condition Eq. (6) to be fulfilled

$$\sigma_{xx}\left(\theta^M\right) = k_{xx}\left(\theta^M\right)E_i\varepsilon_{zz} \geq \sigma_i^c . \tag{31}$$

Combining Eq. (30) and Eq. (31) leads to compare the characteristic interfacial length $L_i^c = E_i G_i^c \Big/ \left(\sigma_i^c\right)^2$ to the structural length βR with

$$\beta = \frac{A\left(\theta^M\right)}{k_{xx}\left(\theta^M\right)^2} . \tag{32}$$

If $L_i^c \geq \beta R$, the energy condition Eq. (30) is governing. The debonding angle at initiation reaches its maximum value θ^M which only depends on the structural geometry. The debonding strain $\varepsilon_D^M = \sqrt{G_i^c \Big/ RE_i A\left(\theta^M\right)}$ does not depend on the interfacial strength. The debonding stress is thus

$$\sigma_D^M = E_c\sqrt{\frac{G_i^c}{RE_i A\left(\theta^M\right)}} , \tag{33}$$

where E_c is the homogenized composite modulus.

If we exclude the presence of residual stress (which will be considered in the next section), it is worthy of note that Eq. (33) is similar to Eq. (1). Further, Eq. (5) indicates that the nucleated interfacial crack is stable since $\left(dG_{inc}(\theta)/d\theta\right)_{\theta=\theta^M} = 0$ implies that

$$G_i\left(\theta^M\right) = G_{inc}(\theta^M) = G_i^c . \tag{34}$$

Then, according to Eq. (5), $G_i\left(\theta\right) < G_i^c$ for $\theta > \theta^M$ which means a priori crack arrest.

If $L_i^c < \beta R$, the debonding angle at initiation $\theta_D < \theta^M$ now depends on the geometry and the interfacial length L_i^c. It is obtained by solving

$$\frac{A(\theta_D)}{k_{xx}(\theta_D)^2} = \frac{L_i^c}{R}. \tag{35}$$

The debonding stress $\sigma_D > \sigma_D^M$ is now

$$\sigma_D = E_c \sqrt{\frac{G_i^c}{R E_i A(\theta_D)}}. \tag{36}$$

In that case [30], the nucleated crack is unstable, at least in an initial phase, since Eq. (5) indicates that

$G_i(S) = G_{inc}(S) + S\left(dG_{inc}(S)/dS\right)$ which leads to $G_i(S) > G_i^c$ as $dG_{inc}(S)/dS > 0$ for $\theta_D < \theta^M$. Finally, Eq. (33) and (36) can be written as

$$\frac{\sigma_D}{\sigma_i^c} = \frac{E_c}{E_i}\sqrt{\frac{L_i^c}{R}}\frac{1}{\sqrt{A(\theta_D)}} \tag{37}$$

with $A(\theta_D)/k_{xx}(\theta_D)^2 = L_i^c/R$ if $L_i^c < \beta R$ and $\theta_D = \theta^M$ if $L_i^c \geq \beta R$.

Fig. 4a depicts the typical evolution of $k_{xx}(\theta)$ and $A(\theta)$ versus the debonding angle. The expected decreasing behavior of the SCF is observed and the presence of a local maximum $A(\theta^M)$ is evidenced. For $\theta > \theta^M$, the normalized IERR is decreasing but a contact model should be used for further calculations as the overlapping of crack faces is detected. Fig. 4b reveals the influence of the particle volume fraction. Increasing V_p enhances the stress concentration and linearly decreases the angle θ^M.

Fig. 5a presents the angle at initiation $\theta_D(L_i^c/R)$ obtained by solving Eq. (35). The angle θ_D increases with L_i^c/R but reaches the value θ^M as soon as $L_i^c/R \geq \beta$. As shown in

Fig. 5b, the structural parameter β decreases with the particle volume fraction and is weakly dependent on the elastic contrast E_p/E_m. Fig. 6a plots the ratio σ_D/σ_i^c as a function of $\sqrt{L_i^c/R}$. A size effect is clearly evidenced which shows that for smaller particles such that $R \le L_i^c/\beta$, the debonding stress scales with $\sqrt{G_i^c/R}$ which is reflected by an increasing linear part in Fig. 6a. For larger particles with $R > L_i^c/\beta$, the debonding stress now depends on G_i^c and σ_i^c. A very low value of the interfacial fracture energy with $L_i^c \to 0$ implies that $\theta_D \to 0$ and the stress condition is dominating with

$$\sigma_D = \frac{E_c \sigma_i^c}{k_{xx}(0) E_i} \tag{38}$$

which corresponds to the horizontal line in Fig. 6a. This plot also depicts the debonding stress provided only by the energy condition Eq. (33) which is similar to Eq. (1) largely used in the literature. It is clear that using only the energy condition leads to underestimate the debonding stress for larger particles. For the typical configuration defined by $E_p/E_M = 10$ and $V_p > 10\%$, results show that this error is less than 1% provided $R \le 2L_i^c/\beta$. The intersection point between the energy condition Eq. (33) and the stress condition Eq. (38) can be easily determined with:

$$\frac{L_i^c}{R} = \frac{A(\theta^M)}{k_{xx}^2(0)} = \gamma^2 . \tag{39}$$

Eq. (39) defines the parameter γ which is plotted versus the particle volume fraction in Fig. 6b. This structural value decreases with V_p and with the elastic contrast E_p/E_m.

Fig. 7 describes the influence of the particle volume fraction on the debonding stress for fixed values of L_i^c/R. For low values of L_i^c/R such that $L_i^c/R < \beta$ for the whole range of investigated particle volume fraction, the decohesion angle θ_D is small and almost independent of L_i^c/R as illustrated in Fig. 5a. However the value $A(\theta_D)$ increases with V_p and the ratio

σ_D/σ_i^c is thus decreasing with V_p according to Eq. (37). For higher values of L_i^c/R such that $L_i^c/R \geq \beta$, Eq. (37) indicates that the ratio σ_D/σ_i^c varies as $E_c/\sqrt{A(\theta^M)}$. As shown by Fig. 4b, the value $A(\theta^M)$ is almost constant with V_p but E_c increases with V_p which explains the increase of the stress ratio. While the failure load increases with the volume fraction of particles V_p for high values of the ratio L_i^c/R, at least in part through an increase in the stiffness of the structure, we draw attention to its unexpected decrease for small values of the ratio. Indeed, increasing the volume fraction of particles also increases the total length of interfaces which is the weak point of the structure in case of very small values of interface toughness, which could explain this phenomenon (see also Fig. 10b).

4.2 Mixed mode conditions

The opening mode is predominant for small values of the debonding angle but it is to be noted that the amplitude of the interfacial shear stress increases with θ_D. The influence of these mixed-mode conditions on the debonding onset can be evaluated with the CC.

The stress condition is modified by introducing an equivalent stress σ_{eq} which combines the interfacial normal and shear stresses $(\sigma_{xx}(\theta), \tau_{xy}(\theta))$. A Coulomb law can be preferred [31] but a quadratic expression is also commonly used [15,32-34]: $\sigma_{eq} = \sqrt{\sigma_{xx}^2 + \tau_{xy}^2/\mu}$ with $\mu = \tau_i^c/\sigma_i^c$ $(\mu \geq 1)$, where τ_i^c is the interfacial shear strength. A high value of μ leads to neglect the influence of shear.

Introducing the SCF $k_{eq}(\theta)$, the stress condition is now given by

$$\sigma_{eq}(\theta) = \sqrt{k_{xx}^2(\theta) + \frac{k_{xy}^2(\theta)}{\mu}} E_i \varepsilon_{zz} = k_{eq}(\theta) E_i \varepsilon_{zz} \geq \sigma_i^c, \quad (40)$$

where $k_{xy}(\theta)=\dfrac{\tau_{xy}(\theta)}{E_i\varepsilon_{zz}}$.

The energy condition $G_{inc}(\theta)\geq G_i^c(\psi)$ must now take into account the dependence of the interfacial fracture energy on the fracture mode mixity angle ψ defined by $\psi(\theta)=\tan^{-1}\left(\tau_{xy}(\theta)/\sigma_{xx}(\theta)\right)$. Using a phenomenological characterization law [35] provides the increase of the interfacial fracture energy versus θ with

$$G_i^c(\theta)=\left[1+\tan^2\left((1-\lambda)\psi(\theta)\right)\right]G_i^c=M(\theta)G_i^c \tag{41}$$

where λ $(0\leq\lambda\leq 1)$ is a material parameter. Setting $\lambda=1$ allows to ignore mode-mixity with $M(\theta)=1$.

The energy condition is thus

$$G_{inc}(\theta)\geq\frac{1}{S(\theta)}\int_0^{\theta}G_i^c\left(\psi(\theta)\right)dS\,. \tag{42}$$

Reminding that $S(\theta)=2\pi R^2(1-\cos\theta)$ leads to

$$G_{inc}(\theta)=RE_i\frac{A(\theta)}{N(\theta)}\varepsilon^2\geq G_i^c,\text{with } N(\theta)=\frac{1}{1-\cos\theta}\int_0^{\theta}M(\theta)\sin\theta d\theta\,. \tag{43}$$

Results indicate that taking into account mode-mixity does not modify the angle θ^M but decreases the structural parameter β which is now given by $\beta=A\left(\theta^M\right)\Big/N\left(\theta^M\right)k_{eq}\left(\theta^M\right)^2$. The debonding stress is now expressed as

$$\frac{\sigma_D}{\sigma_i^c}=\frac{E_c}{E_i}\sqrt{\frac{L_i^c}{R}}\sqrt{\frac{N(\theta_D)}{A(\theta_D)}} \tag{44}$$

with $\dfrac{A(\theta_D)}{N(\theta_D)k_{eq}(\theta_D)^2}=\dfrac{L_i^c}{R}$ if $L_i^c<\beta R$ and $\theta_D=\theta^M$ if $L_i^c\geq\beta R$.

Fig. 8 plots the predictions of the CC obtained with mixed-mode conditions defined by $(\mu=1,\lambda=0.1)$. Comparing with the results that ignore the mixed-mode $(\mu=10,\lambda=1)$, the

debonding angle is higher with mixed-mode conditions (Fig. 8a) but the influence on the debonding stress remains weak (Fig. 8b).

4.3 Presence of residual stresses

If the particle has a larger CTE (α_p) than the matrix (α_m), interfacial tensile stress is generated upon cooling from the fabrication temperature. Introducing the CTE of the composite α_c and $\Delta T < 0$ the temperature change permits to derive the stress and energy conditions for interfacial debonding during the cooling step:

$$\begin{cases} \sigma_{xx}(\theta) = k_{xx}^T(\theta) E_i(-\alpha_c \Delta T) \geq \sigma_i^c, \\ G_{inc}(\theta) = R E_i A^T(\theta)(-\alpha_c \Delta T)^2 \geq G_i^c, \end{cases} \tag{45}$$

where $k_{xx}^T(\theta, V_p, E_p/E_m, \nu_p, \nu_m)$ and $A^T(\theta, V_p, E_p, E_m, \nu_p, \nu_m, \alpha_p, \alpha_m)$ are the corresponding SCF and normalized IERR.

These factors are estimated with the help of a modified finite element procedure which now requires the superposition of three elastic solutions Eq. (21). For this geometry, the stress state at the interface is hydrostatic and k_{xx}^T does not depend on θ. It was checked that the FE model allows to recover the analytical solution of the SCF for a rigid particle embedded within an infinite matrix and submitted to a uniform temperature change [36]. However we detected that the cylindrical cell induces a stress concentration at $\theta = 0$ for higher values of V_p. This artefact limits the use of the cell to low values of the particle volume fraction with $V_p \leq 10\%$. The normalized IERR $A^T(\theta)$ increases monotonically with θ. The maximum angle at

decohesion is thus $\theta_T^M = 90°$. Using the CC provides the debonding angle at initiation by solving

$$\frac{A^T(\theta_D)}{\left(k_{xx}^T\right)^2} = L_i^c / R \quad \text{if} \quad L_i^c < \beta^T R, \tag{46}$$

with $\theta_D = \theta_T^M$ if $L_i^c \geq \beta^T R$ and $\beta^T = A^T\left(\theta_T^M\right) \Big/ k_{xx}^{T\,2}$.

The temperature change $(\Delta T)_D$ at initiation of debonding is given by

$$\frac{-E_i \alpha_c}{\sigma_i^c}(\Delta T)_D = \sqrt{\frac{L_i^c}{R}} \frac{1}{\sqrt{A^T(\theta_D)}} \quad . \tag{47}$$

Fig. 9a illustrates Eq. (47) by plotting $-(\Delta T)_D$ versus L_i^c / R for selected values of the elastic properties of the composite constituents. The curve exhibits two branches defining the stress or the energy dominated domains according to the value of the ratio L_i^c / R.

Debonding upon cooling from the fabrication temperature is not predicted if the temperature change $|\Delta T|$ is lower than the value $|(\Delta T)_D|$ provided by Eq. (47). Superposing now a mechanical tensile load provides the conditions for interfacial debonding taking into account the presence of residual stresses with

$$\begin{cases} \sigma_{xx}(\theta) = k_{xx}(\theta) E_i \varepsilon_{zz} + k_{xx}^T(\theta) E_i(-\alpha_c \Delta T) \geq \sigma_i^c, \\ G_{inc}(\theta) = R E_i \left[A(\theta) \varepsilon_{zz}^2 + A^T(\theta)(\alpha_c \Delta T)^2 \right] \geq G_i^c. \end{cases} \tag{48}$$

The IERR in Eq. (48b) is here simply obtained by adding the values corresponding to the tensile loading (Eq. (29b)) and the temperature change (Eq. (45b)). We have checked numerically that the coupling terms which are present in Eq. (28) can be ignored.

Results show that $\sigma_{xx}(\theta)$ is still a decreasing function of θ and that the IERR possesses a maximum if $\theta = \theta_{TM}^M$. The debonding angle at initiation is obtained by solving

$$\frac{A(\theta_D)}{\left[k_{xx}(\theta_D)\right]^2}\left[1-\kappa k_{xx}^T\right]^2 + A^T(\theta_D)\kappa^2 = \frac{L_i^c}{R}, \tag{49}$$

with $\theta_D \le \theta_{TM}^M$, $\kappa = \sigma^T / \sigma_i^c$ and $\sigma^T = -E_i \alpha_c \Delta T$.

Comparing to Eq. (35) reveals an additional term involving the stress ratio κ. Finally, the debonding strain ε_D can be estimated and the corresponding debonding stress is given by

$$\frac{\sigma_D}{\sigma_i^c} = \frac{E_c}{E_i}\sqrt{\frac{L_i^c}{R}}\frac{1}{\sqrt{A(\theta_D)}}\left[1-\frac{\kappa^2 R}{L_i^c}A^T(\theta_D)\right]^{\frac{1}{2}} \tag{50}$$

It is to be noted that this expression reduces to Eq. (37) if $\kappa = 0$ and that $1 > \frac{\kappa^2 R}{L_i^c}A^T(\theta_D)$ as $|\Delta T| < |\Delta T|_D$. Fig. 9b plots the ratio σ_D / σ_i^c as a function of $\sqrt{L_i^c / R}$ for various values of the stress ratio κ. It is clear that the presence of residual stresses decreases the debonding stress but this influence is weaker for higher values of L_i^c / R as the mechanical loading becomes predominant. Comparing Eq. (50) with Eq. (1) reveals that the additional term σ^T taking into account the thermal residual stresses also depends on the interfacial fracture properties (and not only on the thermal expansion mismatch between the particles and the matrix).

5. Analysis of experimental results

In this section, the numerical results from the previous section are now used to analyze experimental data. More precisely, the objective is to show how the interfacial fracture parameters (σ_i^c, G_i^c) can be extracted from experimental records. Polymer matrices strengthened by glass particles are considered first.

In the study reported by Bai *et al.* [7], samples were made with polyethylene reinforced with glass beads. A coupling agent was used to promote interfacial adhesion and both untreated

(GH1) and treated (GH2) reinforcements were tested. The angle θ_D and the applied stress σ_D at debonding onset were estimated with the help of in situ tensile tests. In this case, the identification procedure is straightforward. Eq. (30) and Eq. (31) respectively provide the estimation of the interfacial strength and toughness with $\sigma_i^c = k_{xx}(\theta_D)\sigma_D$ and $G_i^c = \frac{R}{E_i} A(\theta_D)\sigma_D^2$. Corresponding estimations are indicated in Table 1 for GH1 and GH2 composites. These interfacial properties characterize a very weak interface but it is worthy of note that similar magnitude orders were also determined in [7] as reported in Table 1. It is expected that the CC provides a better accuracy as these authors used more approximate models. As pointed out by the authors, the interfacial debonding is difficult to detect and may occur earlier so that the experimental debonding stress is an upper limit which is consequently also the case for the estimated interfacial properties.

In their experimental work, Cho *et al.* [9] have also observed the nucleation of interfacial debonding within composites made with a vinyl ester resin reinforced with glass particles of various diameters. Their results indicate that the debonding stress can be taken as about 90% (respectively 70%) of the tensile strength of each composite if $R \geq 70$ μm (respectively $R < 70$ μm). Following the procedure proposed by Martin *et al.* [37], Eq. (37) is used to produce isovalues of the debonding stress in the (σ_i^c, G_i^c) plane. For each particle radius, a search procedure then allows to estimate the values of the interfacial parameters which provide the best fit of the predicted values with the experimental data as indicated in Table 1. Fig. 10a plots the predicted ratio σ_D/σ_i^c as a function of $\sqrt{L_i^c/R}$ and reveals that the values $(\sigma_i^c = 62 \text{ MPa}, G_i^c = 35.7 \text{ Jm}^{-2})$ lead to a good agreement for the largest particles $(R \geq 70 \text{ μm})$. The CC predicts a larger applied stress for a small particle $(R = 6 \text{ μm})$. It is very likely that the experimentally found values in this case are not initially caused by

particle/matrix debonding but by matrix cracking. In fact, the values of the debond load are deduced from the loading at final failure (weighted by a coefficient of 70 or 90%) without it being possible in reality to know precisely the origin of the mechanism. The tensile strength of the matrix (50 MPa) is obviously an upper bound for the predicted values for debonding. This upper bound is clearly visible on Fig. 10a.

It reveals difficult to find in the literature experimental data indicating debond thresholds for various particle volume fractions. We use data from Papanicolaou and Bakos [38] who reported the tensile strength of composites made with glass beads embedded in an epoxy resin. Table 1 indicates that various volume fractions up to 30% were used. Based on the observations by Cho *et al.* [9], the debonding stress was taken as 90% (respectively 70%) of the tensile strength if $R \geq 70$ μm (respectively $R < 70$ μm). These experimental data are analyzed with a search procedure (based on Eq. (37)) in order to identify the interfacial parameters (Table 1). Fig. 10b compares the CC prediction of the debonding stress versus the particle volume fraction with the experimental results. As already shown in Fig. 7 and Section 4.1, a low value of the ratio L_i^c / R is required to reproduce the decrease of the debonding stress with V_p .

Finally, we consider ceramic matrix composites reinforced with particles based on the results of Davidge and Green [39]. These authors fabricated several glass composites with a 10% volume fraction of ThO_2 spheres. Several batches with particles of varying radius between $R_{\min} = 22.5$ μm and $R_{\max} = 355$ μm were elaborated with vacuum hot-pressing. Micrographic examination of the specimens after cooling revealed cracks that originate at the matrix/particle interface. The presence of cracks was found dependent on the sphere radius: an upper bound $R \leq R_1$ and a lower bound $R \geq R_2$ respectively define the absence and the presence of cracks. Assuming that the interfacial properties are identical for every batch, these experimental results indicate that the energy condition (which depends explicitly on the particle radius) controls the interfacial debonding. Following Eq. (46), we can thus consider that the debonding angle is

$\theta_D = \theta_T^M$ with $L_i^c \geq \beta^T R$ for $R_{\min} \leq R \leq R_{\max}$. Applying the energy condition Eq. (45b) provides estimations of the interfacial fracture energy with

$$\begin{cases} G_i^c > \left(G_i^c\right)_{\min} = R_1 E_i A^T\left(\theta_T^M\right)\left(-\alpha_c \Delta T\right)^2, \\ G_i^c \leq \left(G_i^c\right)_{\max} = R_2 E_i A^T\left(\theta_T^M\right)\left(-\alpha_c \Delta T\right)^2. \end{cases} \tag{51}$$

An upper bound of the interfacial strength is obtained with the help of the condition $L_i^c \geq \beta^T R_{\max}$ for $\left(G_i^c\right)_{\min} \leq G_i^c \leq \left(G_i^c\right)_{\max}$ which leads to

$$\sigma_i^c \leq \sqrt{\frac{E_i\left(G_i^c\right)_{\min}}{\beta^T R_{\max}}} = \left|E_i \alpha_c \Delta T\right| \sqrt{\frac{R_1}{R_{\max}} \frac{A^T\left(\theta_T^M\right)}{\beta^T}} \ . \tag{52}$$

The estimations of the interfacial properties through Eq. (51) and (52) only require the structural parameters $\left(A^T\left(\theta_T^M\right), \beta^T\right)$ which can be easily computed as described in the previous section. Table 2 reports the values corresponding to the experimental results obtained with two different matrices.

6. Conclusion

Interfacial debonding between stiff particles and a soft matrix submitted to tensile loading is analyzed with a finite fracture mechanics approach. A finite element model of a cylindrical representative cell is used to apply the CC which couples stress and energy conditions. This method does not require any assumption regarding the crack size at debonding onset and is very efficient to derive the debonding stress for various interfacial properties. The key parameters are the length ratio L_i^c / R and the structural parameter β as the condition $L_i^c / R \geq \beta$ delimitates the energy dominant domain for which the debonding stress scales with $\sqrt{G_i^c / R}$. Additional results reveal that the influence of interfacial mixed-mode conditions on

the value of the debonding stress is weak. Taking into account the cooling phase after elaboration at high temperature allows to estimate the amplitude of the temperature change responsible for debonding. Superposing residual stresses and mechanical loading introduces an additional term proportional to the stress ratio κ which decreases the applied stress at debonding. Finally, it is shown that experimental data can be used to estimate bounds or values of the interfacial fracture properties.

References

[1] A.S. Argon, R.E. Cohen, Toughenability of polymers, Polymer. 44 (2003) 6013–6032. https://doi.org/10.1016/S0032-3861(03)00546-9.

[2] B. Cotterell, J.Y.H. Chia, K. Hbaieb, Fracture mechanisms and fracture toughness in semicrystalline polymer nanocomposites, Engineering Fracture Mechanics. 74 (2007) 1054–1078. https://doi.org/10.1016/j.engfracmech.2006.12.023.

[3] M. Taya, S. Hayashi, A.S. Kobayashi, H.S. Yoon, Toughening of a Particulate-Reinforced Ceramic-Matrix Composite by Thermal Residual Stress, J American Ceramic Society. 73 (1990) 1382–1391. https://doi.org/10.1111/j.1151-2916.1990.tb05209.x.

[4] Y.-W. Bao, C.-C. Liu, J.-L. Huang, Effects of residual stresses on strength and toughness of particle-reinforced TiN/Si_3N_4 composite: Theoretical investigation and FEM simulation, Materials Science and Engineering: A. 434 (2006) 250–258. https://doi.org/10.1016/j.msea.2006.06.136.

[5] J. Chen, G.-T. Wang, Z.-Z. Yu, Z. Huang, Y.-W. Mai, Critical particle size for interfacial debonding in polymer/nanoparticle composites, Composites Science and Technology. 70 (2010) 861–872. doi:10.1016/j.compscitech.2010.02.004.

[6] P. Vollenberg, D. Heikens, H.C.B. Ladan, Experimental determination of thermal and adhesion stress in particle filled thermoplasts, Polym. Compos. 9 (1988) 382–388. https://doi.org/10.1002/pc.750090603.

[7] S.-L. Bai, M. Wang, X.-F. Zhao, Interfacial debonding behavior of a rigid particle-filled polymer composite, Composite Interfaces. 10 (2003) 243–253. https://doi.org/10.1163/156855403765826892.

[8] J.A. Tjernlund, E. Kristofer Gamstedt, P. Gudmundson, Length-scale effects on damage development in tensile loading of glass-sphere filled epoxy, International Journal of Solids and Structures. 43 (2006) 7337–7357. https://doi.org/10.1016/j.ijsolstr.2006.05.026.

[9] J. Cho, M.S. Joshi, C.T. Sun, Effect of inclusion size on mechanical properties of polymeric composites with micro and nano particles, Composites Science and Technology. 66 (2006) 1941–1952. https://doi.org/10.1016/j.compscitech.2005.12.028.

[10] D. Hosseinpour, J.C. Berg, Stress/strain development around a spherical inclusion in a polymeric matrix: The effects of particle and matrix mechanical characteristics and thermal expansivity difference, J. Appl. Polym. Sci. 126 (2012) 678–685. https://doi.org/10.1002/app.36855.

[11] B. Pukánszky, G. Vörös, Stress distribution around inclusions, interaction, and mechanical properties of particulate-filled composites: Stress Distribution Around Inclusions, Polym Compos. 17 (1996) 384–392. https://doi.org/10.1002/pc.10625.

[12] A.N. Gent, Detachment of an elastic matrix from a rigid spherical inclusion, J Mater Sci. 15 (1980) 2884–2888. https://doi.org/10.1007/BF00550559.

[13] J.-K. Chen, Z. Huang, S.-L. Bai, Y. Liu, Theoretical analysis on the local critical stress and size effect for interfacial debonding in particle reinforced rheological materials, Acta Mechanica Solida Sinica. 12 (1999) 1–8.

[14] J. Chen, Z. Huang, J. Zhu, Size effect of particles on the damage dissipation in nanocomposites, Composites Science and Technology. 67 (2007) 2990–2996. https://doi.org/10.1016/j.compscitech.2007.05.020.

[15] I.G. García, V. Mantič, E. Graciani, A model for the prediction of debond onset in spherical-particle-reinforced composites under tension. Application of a coupled stress and energy criterion, Composites Science and Technology. 106 (2015) 60–67. doi:10.1016/j.compscitech.2014.10.010.

[16] T. Gentieu, J. Jumel, A. Catapano, J. Broughton, Size effect in particle debonding: Comparisons between finite fracture mechanics and cohesive zone model, Journal of Composite Materials. (2018) 002199831881647. doi:10.1177/0021998318816471.

[17] D. Leguillon, Strength or toughness? A criterion for crack onset at a notch, European Journal of Mechanics - A/Solids. 21 (2002) 61–72. https://doi.org/10.1016/S0997-7538(01)01184-6.

[18] P. Cornetti, N. Pugno, A. Carpinteri, D. Taylor, Finite fracture mechanics: A coupled stress and energy failure criterion, Engineering Fracture Mechanics. 73 (2006) 2021–2033. https://doi.org/10.1016/j.engfracmech.2006.03.010.

[19] E. Martin, D. Leguillon, Energetic conditions for interfacial failure in the vicinity of a matrix crack in brittle matrix composites, International Journal of Solids and Structures. 41 (2004) 6937–6948. https://doi.org/10.1016/j.ijsolstr.2004.05.044.

[20] A. Doitrand, E. Martin, D. Leguillon, Numerical implementation of the coupled criterion: Matched asymptotic and full finite element approaches, Finite Elements in Analysis and Design. 168 (2020) 103344. https://doi.org/10.1016/j.finel.2019.103344.

[21] D. Quesada, D. Leguillon, C. Putot, Multiple failures in or around a stiff inclusion embedded in a soft matrix under a compressive loading, European Journal of Mechanics - A/Solids. 28 (2009) 668–679. https://doi.org/10.1016/j.euromechsol.2009.03.001.

[22] J.C. Smith, Experimental values for the elastic constants of a particulate-filled glassy polymer, Journal of Research of the National Bureau of Standards - A. 80A (1976) 45. https://doi.org/10.6028/jres.080A.008.

[23] B.D. Agarwal, L.J. Broutman, Three-dimensional finite element analysis of spherical particle composites, Fibre Science and Technology. 7 (1974) 63-77.

[24] L. Banks-Sills, V. Leiderman, D. Fang, On the effect of particle shape and orientation on elastic properties of metal matrix composites, Composites Part B: Engineering. 28 (1997) 465–481. https://doi.org/10.1016/S1359-8368(96)00068-6.

[25] I.G. García, V. Mantič, E. Graciani, Debonding at the fibre–matrix interface under remote transverse tension. One debond or two symmetric debonds?, European Journal of Mechanics - A/Solids. 53 (2015) 75–88. https://doi.org/10.1016/j.euromechsol.2015.02.007.

[26] J.N. Goodier, Concentration of Stress Around Spherical and Cylindrical Inclusions and Flaws, J. Appl. Mech. 55 (1933) 39-44.

[27] T.T. Wang, M. Matsuo, T.K. Kwei, Criteria of Craze Initiation in Glassy Polymers, Journal of Applied Physics. 42 (1971) 4188–4196. https://doi.org/10.1063/1.1659752.

[28] F. París, E. Correa, V. Mantič, Kinking of Transversal Interface Cracks Between Fiber and Matrix, Journal of Applied Mechanics. 74 (2007) 703–716. https://doi.org/10.1115/1.2711220.

[29] P. Weißgraeber, S. Hell, W. Becker, Crack nucleation in negative geometries, Engineering Fracture Mechanics. 168 (2016) 93–104. https://doi.org/10.1016/j.engfracmech.2016.02.045.

[30] A. Doitrand, R. Estevez, D. Leguillon, Comparison between cohesive zone and coupled criterion modeling of crack initiation in rhombus hole specimens under quasi-static compression, Theoretical and Applied Fracture Mechanics. 99 (2019) 51–59. https://doi.org/10.1016/j.tafmec.2018.11.007.

[31] J. Fitoussi, G. Guo, D. Baptiste, Determination of a tridimensional failure criterion at the fibre/matrix interface of an organic-matrix/discontinuous-reinforcement composite, Composites Science and Technology. 56 (1996) 755–760. https://doi.org/10.1016/0266-3538(96)00017-6

[32] S. Ogihara, J. Koyanagi, Investigation of combined stress state failure criterion for glass fiber/epoxy interface by the cruciform specimen method, Composites Science and Technology. 70 (2010) 143–150. https://doi.org/10.1016/j.compscitech.2009.10.002.

[33] F. Greco, L. Leonetti, P. Lonetti, A two-scale failure analysis of composite materials in presence of fiber/matrix crack initiation and propagation, Composite Structures. 95 (2013) 582–597. https://doi.org/10.1016/j.compstruct.2012.08.035.

[34] P.A. Carraro, M. Quaresimin, Modelling fibre–matrix debonding under biaxial loading, Composites Part A: Applied Science and Manufacturing. 61 (2014) 33–42. https://doi.org/10.1016/j.compositesa.2014.01.016.

[35] J.W. Hutchinson, Z. Suo, Mixed Mode Cracking in Layered Materials, in: J.W. Hutchinson, T.Y. Wu (Eds.), Advances in Applied Mechanics, Elsevier, 1991: pp. 63–191. https://doi.org/10.1016/S0065-2156(08)70164-9.

[36] J. Selsing, Internal stresses in ceramics, J American Ceramic Society. 44 (1961) 419–419. https://doi.org/10.1111/j.1151-2916.1961.tb15475.x.

[37] E. Martin, D. Leguillon, O. Sevecek, R. Bermejo, Understanding the tensile strength of ceramics in the presence of small critical flaws, Engineering Fracture Mechanics. 201 (2018) 167–175. https://doi.org/10.1016/j.engfracmech.2018.06.021.

[38] G.C. Papanicolaou, D. Bakos, The Influence of the Adhesion Bond between Matrix and Filler on the Tensile Strength of Particulate-Filled Polymers, Journal of Reinforced Plastics and Composites. 11 (1992) 104–126. https://doi.org/10.1177/073168449201100201.

[39] R.W. Davidge, T.J. Green, The strength of two-phase ceramic/glass materials, Journal of Materials Science. 3 (1968) 629–634.

Table 1

Analysis of experimental data (polymer matrices reinforced with glass particles)

	E_p (GPa)	ν_p	E_m (GPa)	ν_m	V_p (%)	R (μm)	θ_D (1) (°)	σ_D (1) (MPa)	σ_D (2) (MPa)	σ_i^c (1) (MPa)	G_i^c (1) (Jm^{-2})	σ_i^c (2) (MPa)	G_i^c (2) (Jm^{-2})
[7]	52	0.22	1.03	0.38	5								
GH1						10	23	3.81		6.6	$28.0\ 10^{-3}$	6.0	$65.3\ 10^{-3}$
GH2						13	20.5	5.0		8.6	$63.0\ 10^{-3}$	8.3	$133.4\ 10^{-3}$
[9]	70	0.25	3.5	0.35	5						25-50	62	35.7
						6		46.2	168.7				
						72		51.2	53.4				
						210		42.9	38.4				
						521		32.7	34.4				
[38]	53.3	0.27	4.21	0.35		108						71.1	1.0
					5			47.6	39.0				
					10			40.7	38.7				
					15			37.1	38.0				
					20			34.8	37.1				
					25			33.1	36.0				
					30			31.8	34.6				
						10.5							
					5			56.7	51.8			93.3	0.8
					10			52.2	51.3				
					15			49.8	50.5				
					20			48.1	49.5				
					25			46.8	48.1				
					30			45.8	46.5				

(1) experimental value - (2) identified value

Table 2

Analysis of experimental data (glass matrices reinforced with thoria particles [39])

	E_p (GPa)	ν_p	α_p (10^{-6} °C^{-1})	E_m (GPa)	ν_m	α_m (10^{-6} °C^{-1})	V_p (%)	ΔT (°C)	R_1 (μm)	R_2 (μm)	$\left(\sigma_i^c\right)_{\max}$ (MPa)	$\left(G_i^c\right)_{\min}$ (Jm^{-2})	$\left(G_i^c\right)_{\max}$ (Jm^{-2})
G1	250	0.275	8.7	70	0.2	3.6	10	-545	29.5	41.5	64	8.3	11.6
G2	250	0.275	8.7	70	0.2	5.4	10	-500	97.5	137.5	68.7	9.65	13.6

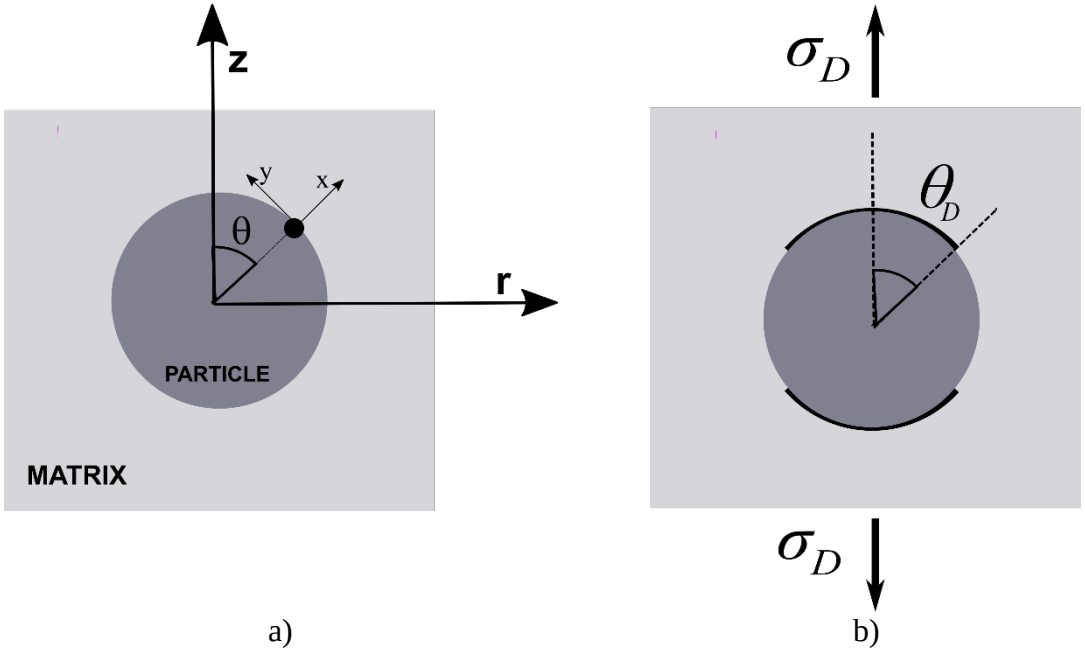

a) b)

Fig. 1: a) A spherical particle bonded to a surrounding matrix and subjected to a tensile loading in the *z* direction, b) Nucleation of interfacial debonding (angle θ_D) for an applied debonding stress σ_D.

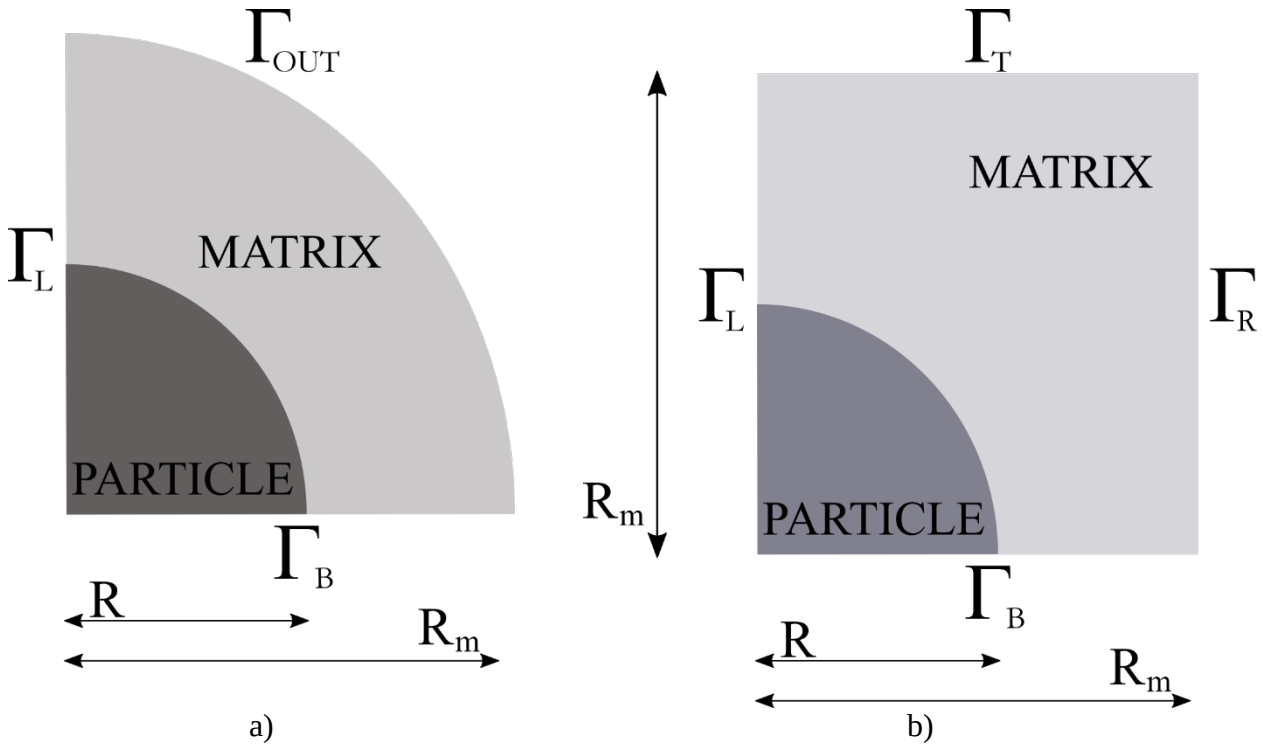

Fig. 2: Representative volume element with a) spherical geometry, b) cylindrical geometry.

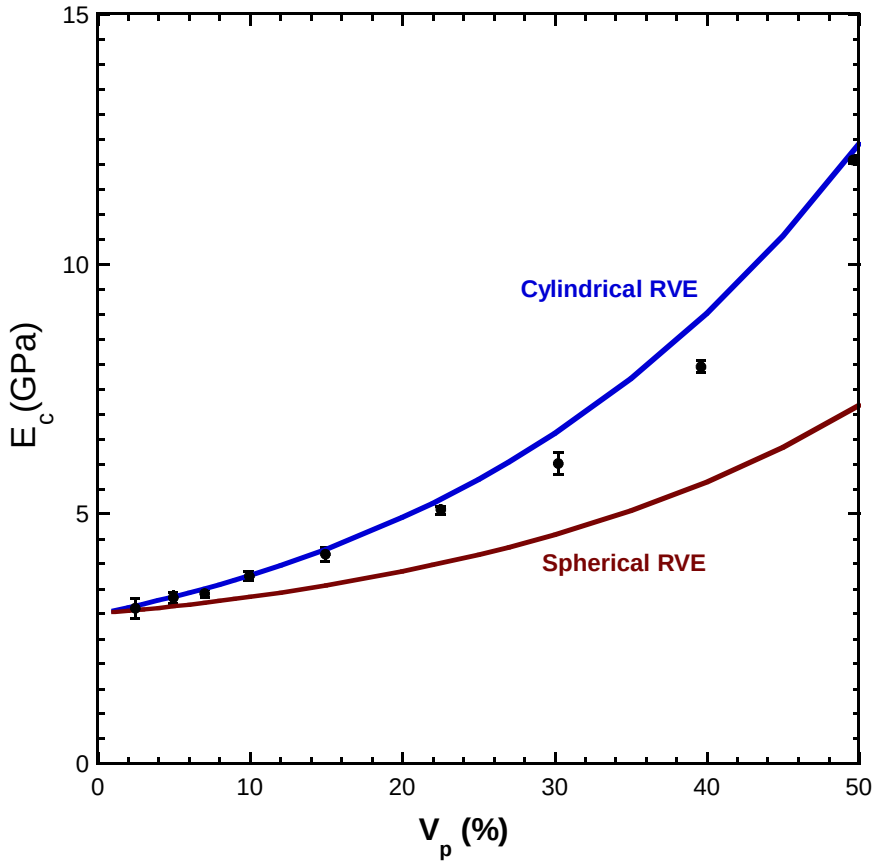

Fig. 3: Young's modulus of a composite made with small glass spheres imbedded in an epoxy polymer matrix [22]: comparison of the experimental data (black dots) with the prediction of the spherical (red line) and cylindrical (blue line) RVEs with $E_p = 76$ GPa, $\nu_p = 0.23$, $E_m = 3$ GPa, $\nu_m = 0.4$.

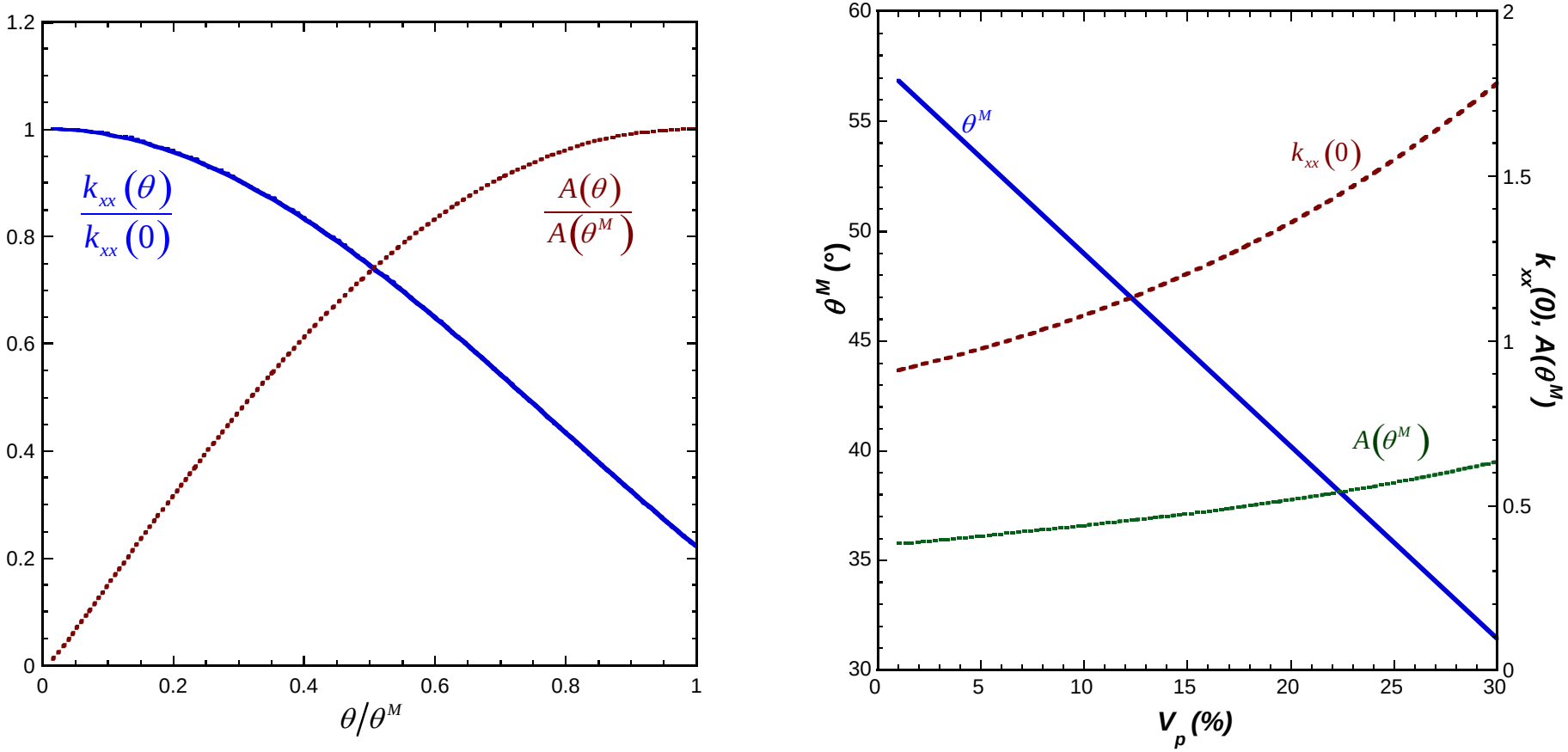

a) b)

Fig. 4: a) Evolution of the stress concentration factor $k_{xx}(\theta)$ and the incremental energy release rate $A(\theta)$ versus the debonding angle θ for $V_p = 1\%$, b) Maximum debonding angle θ^M, stress concentration factor $k_{xx}(0)$ and normalized incremental energy release rate $A(\theta^M)$ versus the particle volume fraction V_p. These data are computed for $E_p/E_m = 10, \nu_p = 0.2, \nu_m = 0.3$.

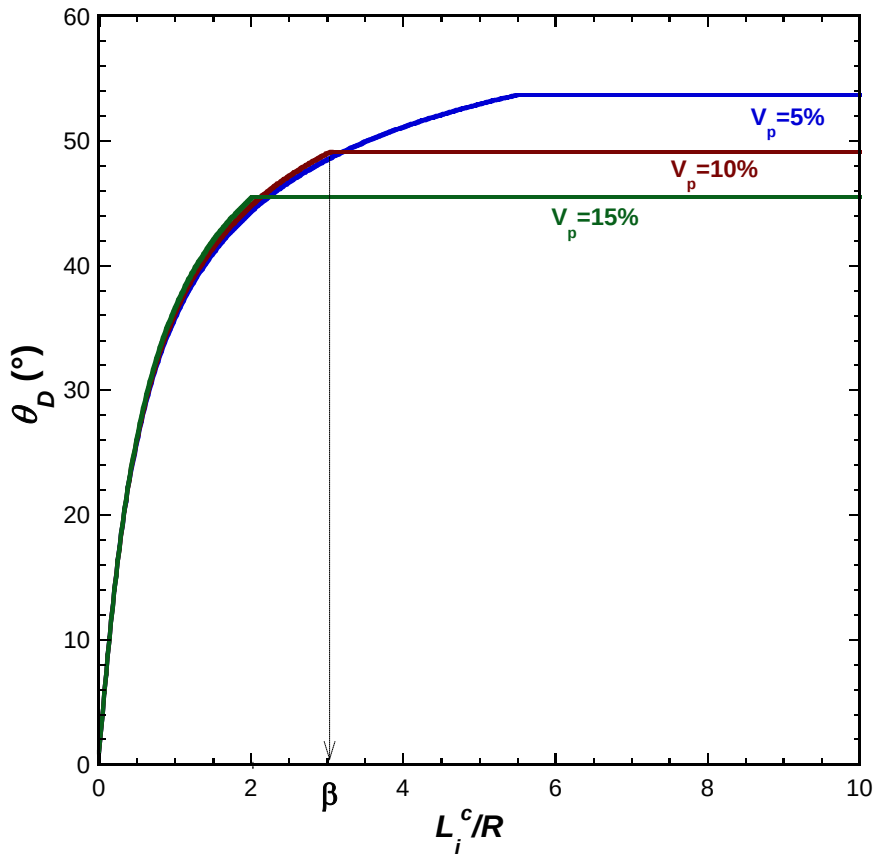

a)

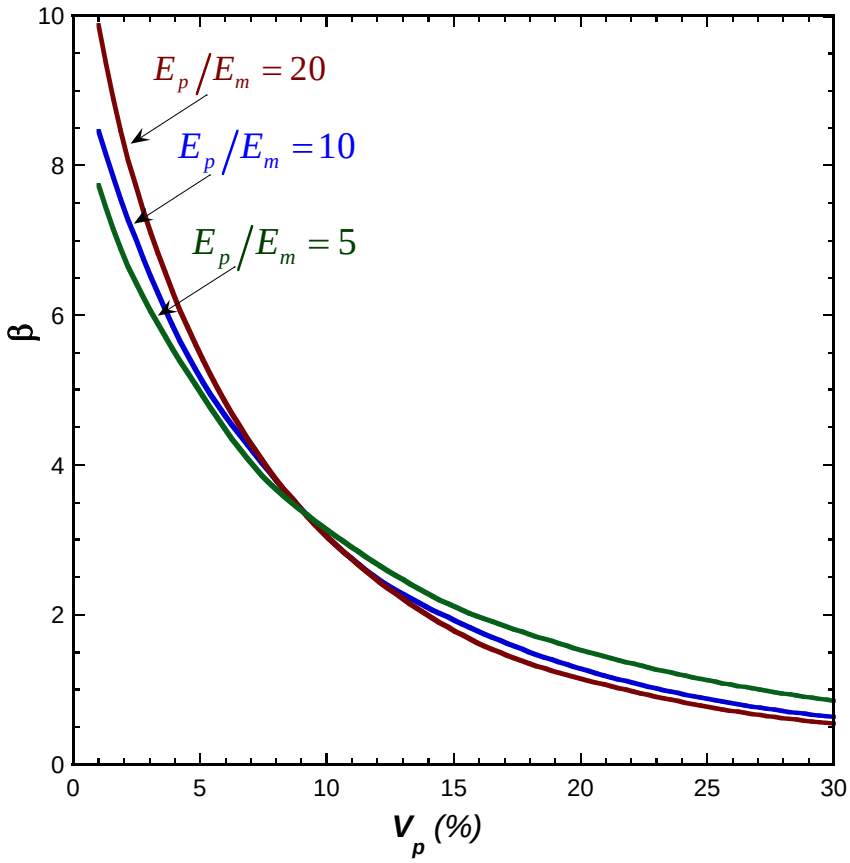

b)

Fig. 5: a) Debonding angle θ_D at crack onset versus the ratio of the interfacial length L_i^c over the particle radius R for various values of the particle volume fraction with $E_p/E_m = 10, \nu_p = 0.2, \nu_m = 0.3$, b) Structural parameter β Eq. (32) versus the particle volume fraction V_p for various values of the elastic contrast with $(\nu_p = 0.2, \nu_m = 0.3)$.

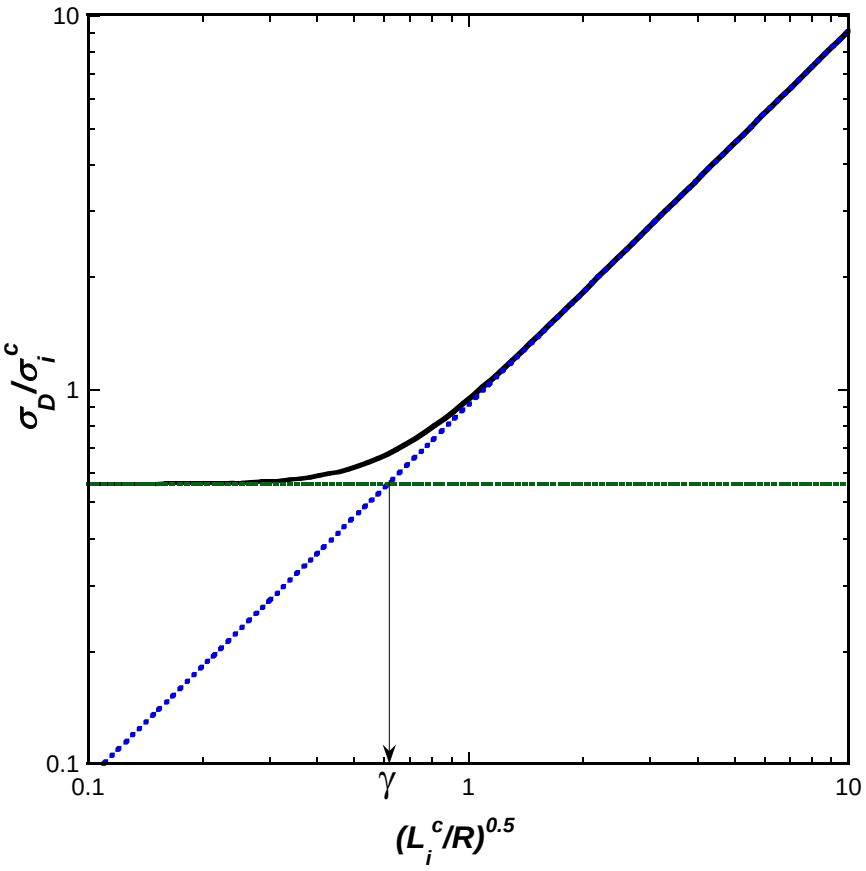

a)

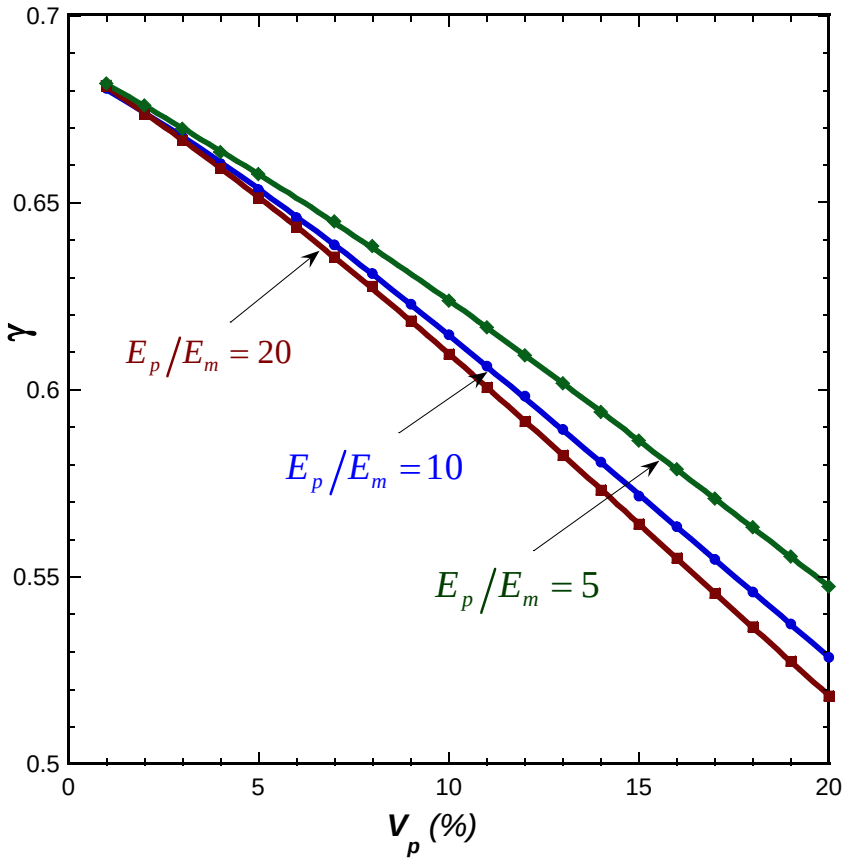

b)

Fig. 6: a) Debonding stress ratio σ_D/σ_i^c at crack onset versus $\sqrt{L_i^c/R}$ for V_p=10% with $E_p/E_m = 10, \nu_p = 0.2, \nu_m = 0.3$; the blue and the green line respectively plots the energy condition Eq. (33) and the stress condition Eq. (38) , b) Structural parameter γ Eq. (39) versus the particle volume fraction V_p for various values of the elastic contrast with $\left(\nu_p = 0.2, \nu_m = 0.3\right)$.

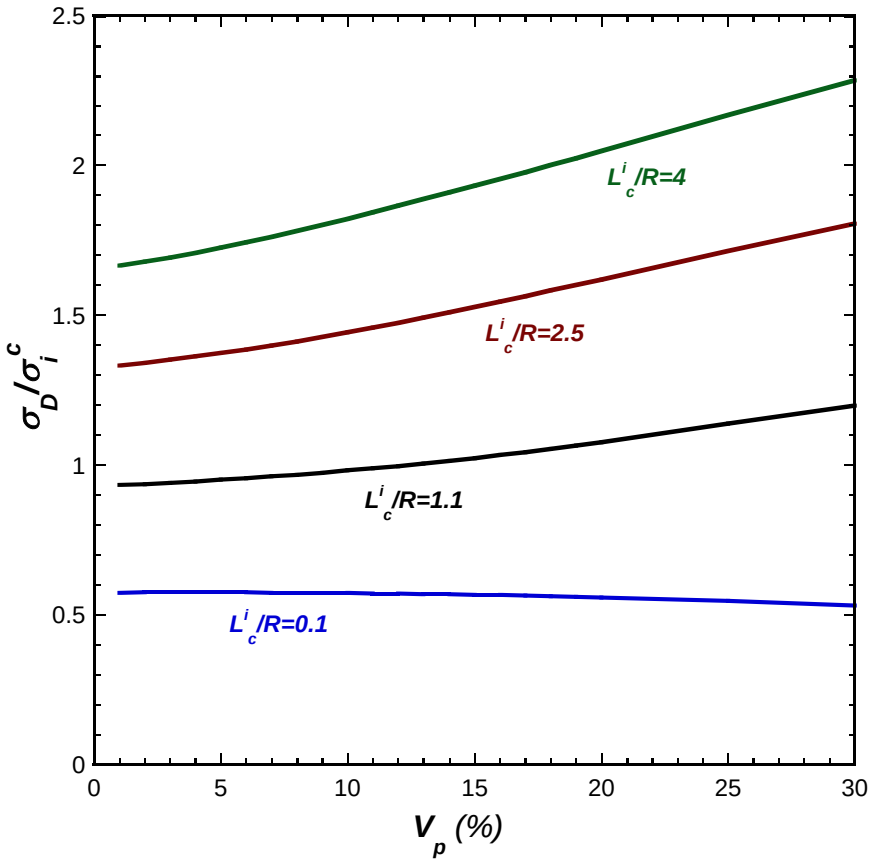

Fig. 7: a) Debonding stress ratio σ_D/σ_i^c at crack onset versus the particle volume fraction for various values of the ratio L_i^c/R with $E_p/E_m = 10, \nu_p = 0.2, \nu_m = 0.3$.

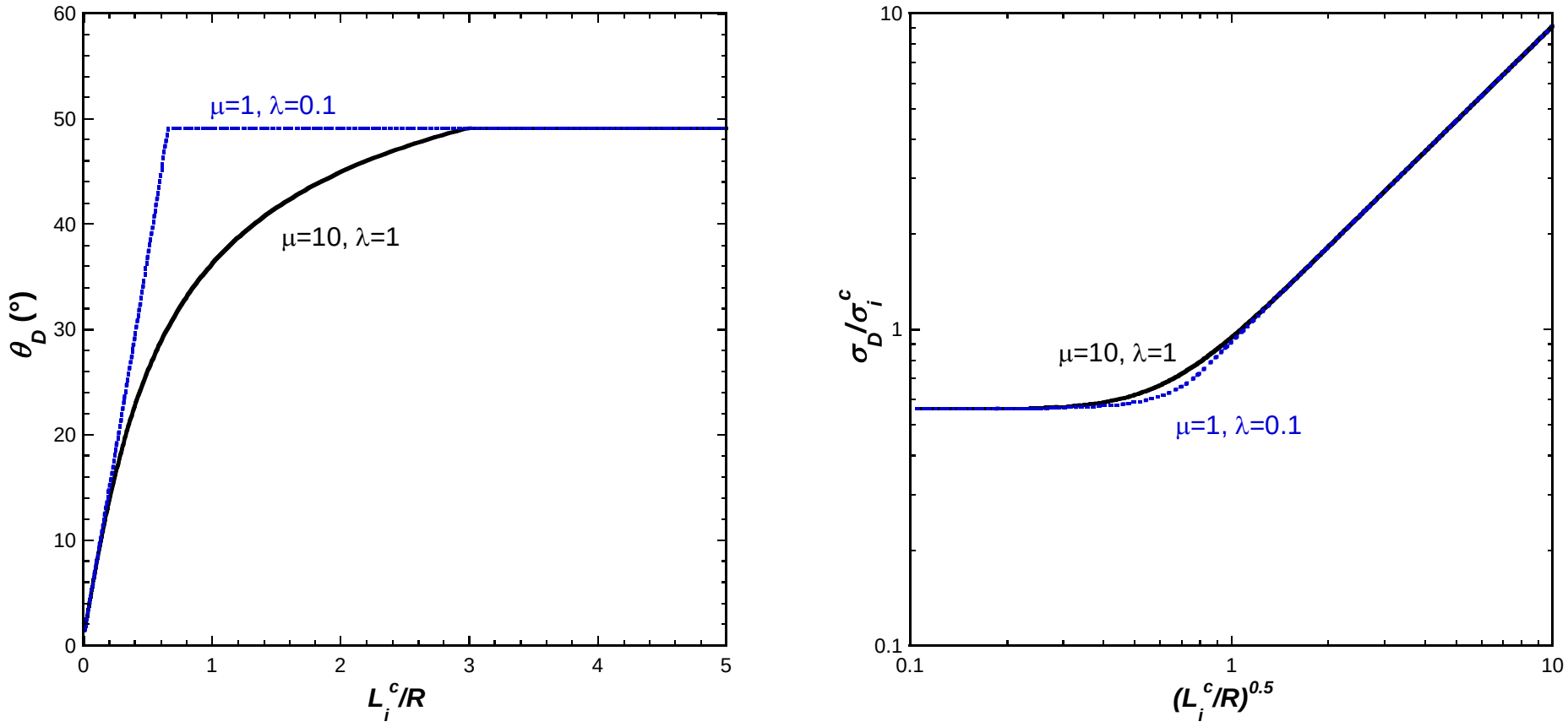

a) b)

Fig. 8: Influence of the mixed mode conditions defined by $(\mu = 10, \lambda = 1)$ and $(\mu = 1, \lambda = 0.1)$ with $E_p/E_m = 10, \nu_p = 0.2, \nu_m = 0.3, V_p = 10\%$: a) Debonding angle θ_D at crack onset versus the ratio L_i^c/R, b) Debonding stress ratio σ_D/σ_i^c at crack onset versus $\sqrt{L_i^c/R}$.

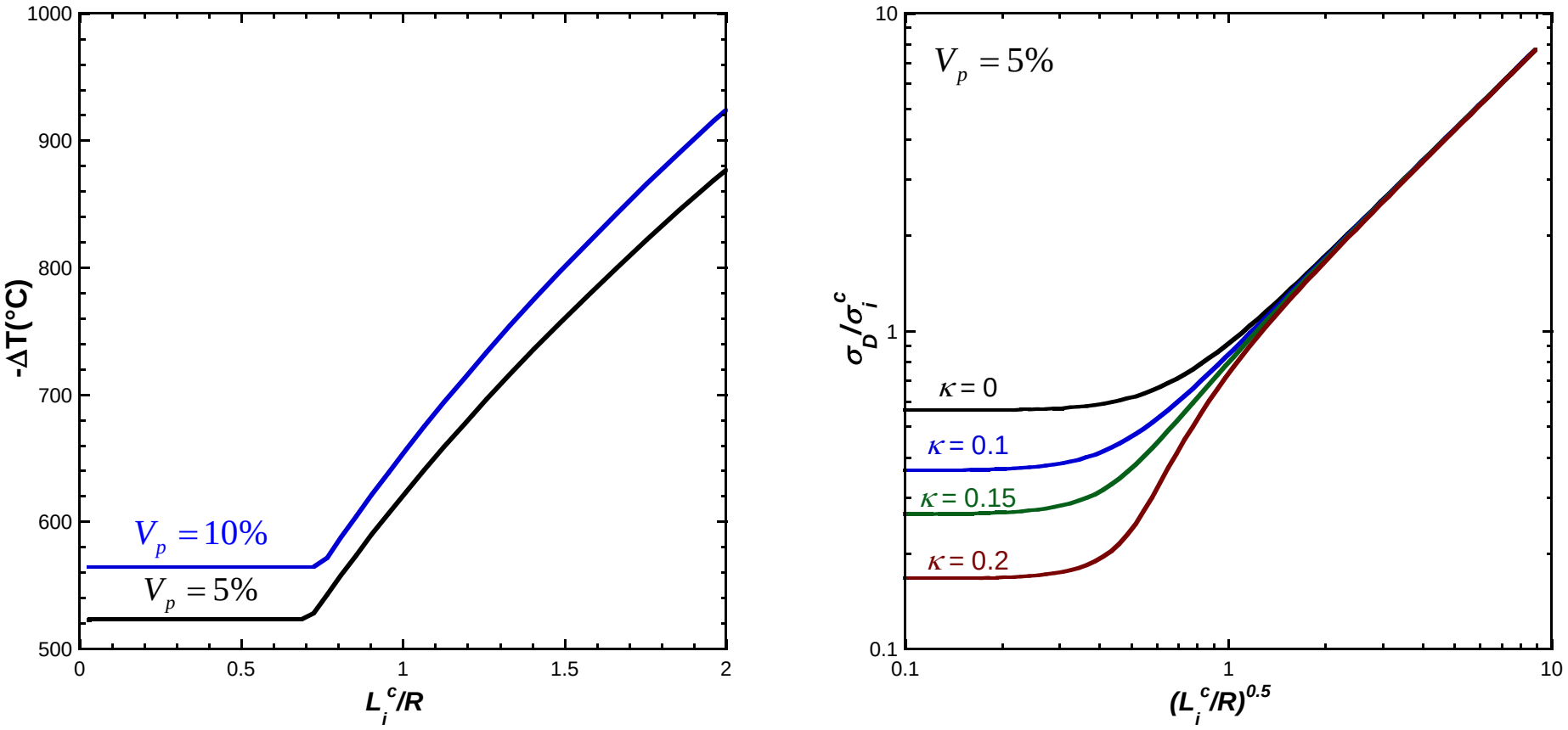

a) b)

Fig. 9: Influence of residual stresses a) Temperature change at initiation of debonding versus the ratio L_i^c/R for two values of the particle volume fraction, b) Debonding stress ratio σ_D/σ_i^c at crack onset versus $\sqrt{L_i^c/R}$ for various values of the residual stress ratio κ and $V_p = 10\%$. The material data are $E_p = 100$ GPa, $\nu_p = 0.2$, $\alpha_p = 10\text{E}-06\,°\text{C}^{-1}$, $E_m = 10$ GPa, $\nu_m = 0.3$, $\alpha_m = 1\text{E}-06\,°\text{C}^{-1}$.

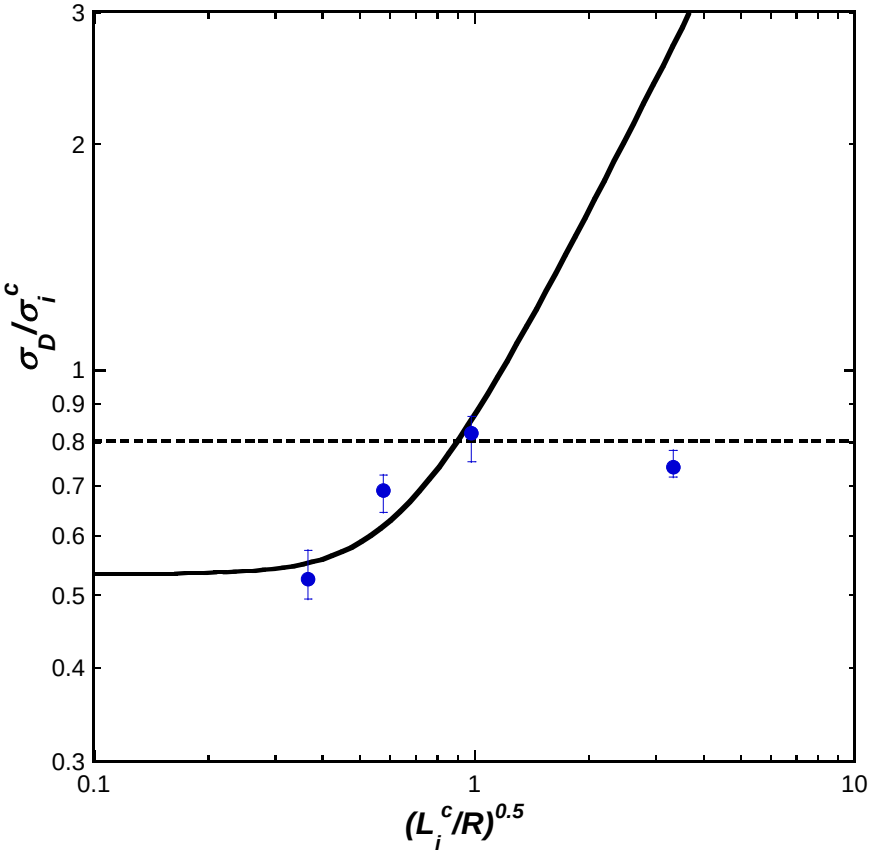

a)

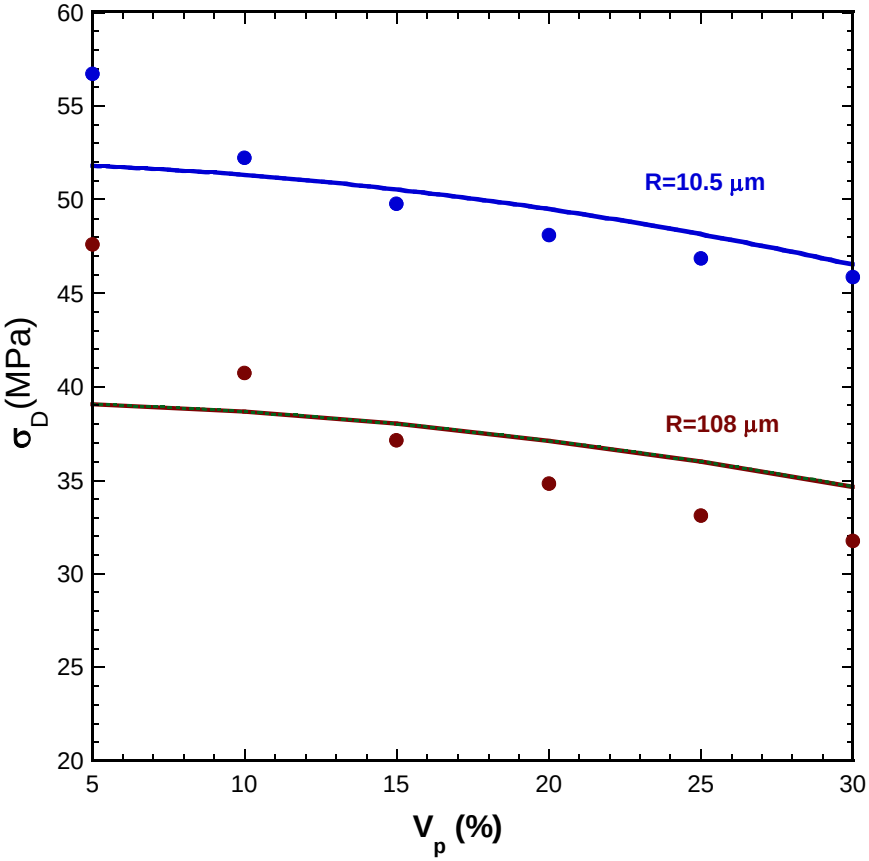

b)

Fig. 10: Analysis of experimental data (points) with the CC (solid line) in order to identify the interfacial fracture parameters (Table 1): a) Debonding stress ratio σ_D/σ_i^c at crack onset versus $\sqrt{L_i^c/R}$ [9]; the dotted line plots the ratio of the matrix tensile strength over the identified interfacial strength, b) Debonding stress versus the particle volume fraction for two values of the particle radius $R=10.5$ µm and $R=108$ µm [38].